Schweizerischer Erdbebendienst
Service Sismologique Suisse
Servizio Sismico Svizzero
Swiss Seismological Service

ETH zürich

Mauren - Feuerwehr, FL (SMFL)

SITE CHARACTERIZATION REPORT

Jan BURJÁNEK, Manuel HOBIGER, Stefano MARANÒ, Donat FÄH

Sonneggstrasse 5 CH-8092 Zürich Switzerland; E-mail: burjanek@sed.ethz.ch

Last modified : August 28, 2015

Abstract

Ambient vibration array measurements were performed to characterize the site Mauren, in Liechtenstein. The site, where the new strong motion station SMFL was installed, is located on the loose alluvia of the Rhine valley. The new station was installed in the frame of the Renewal of strong motion seismic network in the Principality Liechtenstein project. In order to characterize the velocity profile under the station, array measurements with a $400\,\mathrm{m}$ aperture were performed. The measurements were successful and allowed deriving a velocity model for this site. We found a first layer of approximately $12\,\mathrm{m}$ with extremely low shear wave velocities of about $70\,\mathrm{m/s}$ corresponding to unconsolidated soil. A rapid increase of velocities to $300-400\,\mathrm{m/s}$ is found at depths of $12-15\,\mathrm{m}$. Below the velocity is increasing up $500-900\,\mathrm{m/s}$ down to the bedrock. The bedrock depth is not well constrained, but the data suggest the minimum depth of $100\,\mathrm{m}$.
$V_{s,30}$ is $134\,\mathrm{m/s}$ would generally correspond to ground type D in the Eurocode 8 [CEN, 2004], and D for the SIA261 [SIA, 2014]. However, the special ground types S1, S2 of Eurocode 8 or type F of the SIA261 [SIA, 2014] should be consider in this case, as the first layer is relatively thick ($12\,\mathrm{m}$) and does not show normal consolidation. A further geotechnical study (like CPT) of the uppermost layer would be required for the more specific classification. The theoretical 1D SH transfer function and impedance contrast of the quarter-wavelength velocity computed from the inverted profiles show significant amplifications at clearly defined resonance frequencies. Recordings on the new station will allow to compare to these simple models.

Contents

1 Introduction

The station SMFL (Mauren - Feuerwehr, FL) is part of the strong motion network of the Principality Liechtenstein, and is run within the Swiss Strong Motion Network (SSMNet). SMFL has been installed in the framework of the Renewal of strong motion seismic network in the Principality Lichtenstein project in 2014, replacing the SNEW (Nendeln, Liechtenstein) dial-up station . This project includes also the site characterization. Passive array measurements have been selected as a standard tool to investigate these sites. An array measurement was carried out on 10th February 2015 in the rural area, close to the Firestation of the Mauren municipality (Fig. 1). The array consisted of five eccentric rings (polygons). The centre of the smallest ring was close to SMFL, whereas SMFL is located rather at vertices of outer rings. Such irregular configuration was selected in order to characterize the velocity profile under the SMFL station and reducing the influence of local sources due to the road maintenance depot which is close by. This report presents the measurement setup, the results of the H/V analysis and of the array processing of the surface waves (dispersion curves). Then, an inversion of these results into velocity profiles is performed. Standard parameters are derived to evaluate the amplification at this site.

Staat	City	Location	Station code	Site type	Slope
Liechtenstein	Mauren	Feuerwehr	SMFL	Alluvial plain	Flat

Table 1: Main characteristics of the study-site.

Figure 1: Picture of the site.

2 Geology

The geological map indicates (Fig. 2) that the site is located on quaternary alluvial sediments of the Rhine river. Below, layers of recent moraines and former Rhine glacier moraines are expected. The bedrock consits of the Vorarlberger Flysch unit and Cretaceous limestones, as the dividing line between the two units is likely beneath the basin. The station is located almost in the middle of the basin where resonance from the Quaternary sediments is expected.

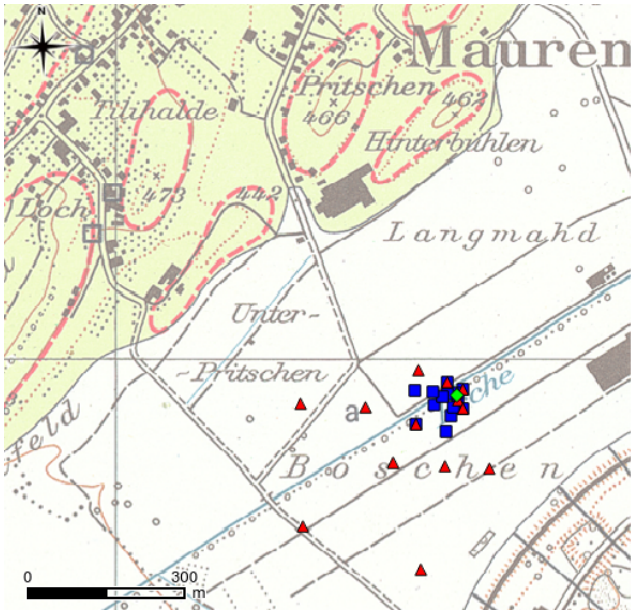

Figure 2: Geological map of the area of station SMFL (green diamond) including the array (blue and red symbols). The white color refers to alluvia and the green area to morraines.

3 Experiment description

3.1 Ambient Vibrations

The ground surface is permanently subjected to ambient vibrations due to:

- natural sources (ocean and large-scale atmospheric phenomena) below 1 Hz,
- local meteorological conditions (wind and rain) at frequencies around 1 Hz ,
- human activities (industrial machines, traffic…) at frequencies above 1 Hz [Bonnefoy-Claudet et al., 2006].

The objective of the measurements is to record these ambient vibrations and to use their propagation properties to infer the underground structure. First, the polarization of the recorded waves (H/V ratio) is used to derive the resonance frequencies of the soil column. Second, the arrival time delays at many different stations are used to derive the velocity of surface waves

at different frequencies (dispersion). The information (H/V, dispersion curves) is then used to derive the properties of the soil column using an inversion process.

3.2 Equipment

For these measurements 12 Quanterra Q330 dataloggers named NR01 to NR12 and 14 Lennartz 3C 5 s seismometers were available (see Tab. 2). Each datalogger can record on 2 ports A (channels EH1, EH2, EH3 for Z, N, E directions) and B (channels EH4, EH5, EH6 for Z, N, E directions). Time synchronization was ensured by GPS. The sensors were placed on a metal tripod, in a $20\,\mathrm{cm}$ deep hole, when necessary, for better coupling with the ground.

Digitizer	**Model**	**Number**	**Resolution**
	Quanterra Q330	12	$24\,\mathrm{bits}$
Sensor type	**Model**	**Number**	**Cut-off frequency**
Velocimeter	Lennartz 3C	14	$0.2\,\mathrm{Hz}$

Table 2: Equipment used.

3.3 Geometry of the arrays

Two array configurations were used. In the first configuration, 3 excentric rings of approximately 10, 25 and $60\,\mathrm{m}$ radius were deployed for a total of 14 sensors. The SMFL station is close to the center of the smallest ring. The configuration is quite irregular because of many obstacles (trees, irrigation channels, fences). The second configuration includes two excentric outer rings of 100 and $200\,\mathrm{m}$ respectively (plus the central station of the first ring and few stations of the first configuration in the vicinity), again 14 sensors in total. The minimum interstation distance and the aperture are therefore 10 and $120\,\mathrm{m}$ and 10 and $400\,\mathrm{m}$, respectively. The experimental setup is displayed in Fig. 3. The final usable datasets are detailed in section 4.2.

3.4 Positioning of the stations

The sensor coordinates were measured using a differential GPS device (Leica Viva GS10), including only a rover station and using the Real Time Kinematic technique provided by Swisstopo. It allows an absolute positioning with an accuracy better than $6\,\mathrm{cm}$ on the Swissgrid. This accuracy was reached for all stations.

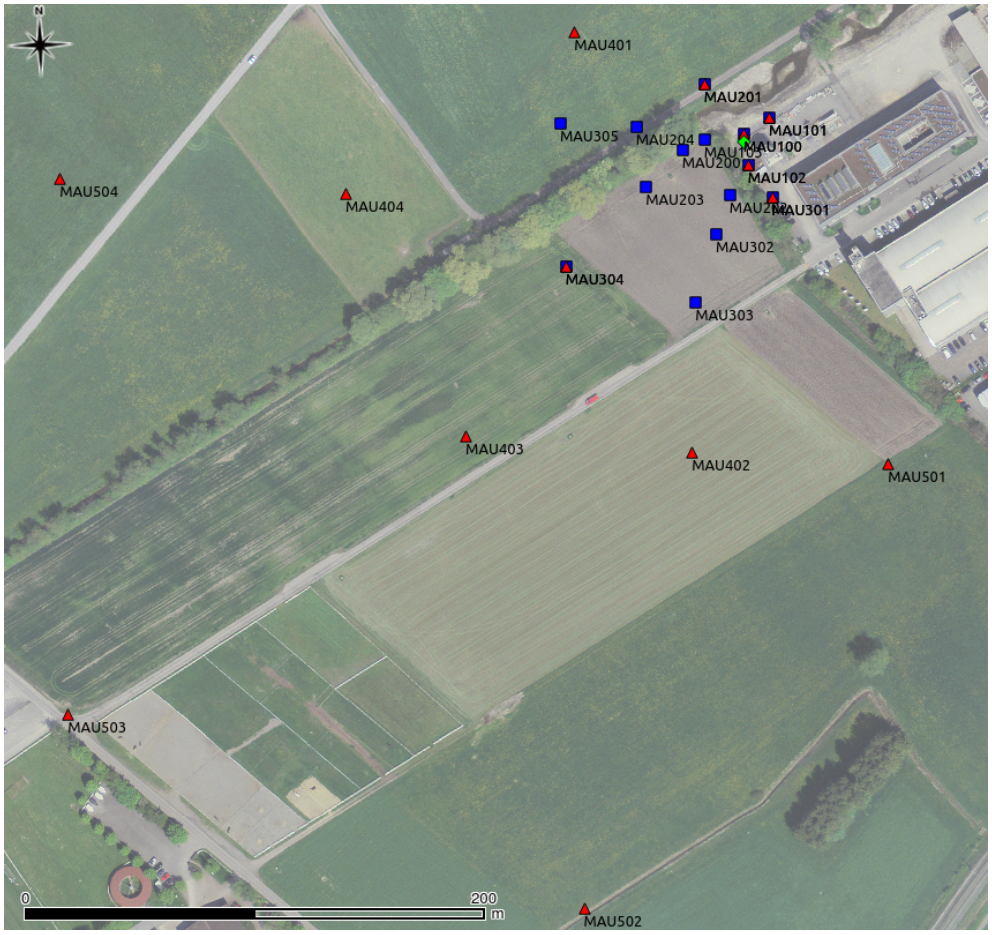

Figure 3: Geometry of the arrays. Blue squares refer to the first configuration, red triangles refer to the second configuration, and green diamond to the SMFL station.

4 Data quality

4.1 Usable data

The largest time windows were extracted, for which all the sensors of the array were correctly placed and the GPS synchronization was ensured. Recordings are generally consistent. Incoherent high amplitude signals are mainly due to the differential GPS measurement, which took longer than usual (almost 2 hours), because of the connectivity issues. For the second configuration, higher noise levels are present at station MAU503, which is close to a relatively busy road.

Orientations of the sensors were checked by maximizing the correlation with the central station at low frequencies [Poggi et al., 2012b]. However, this was not successful, since the recordings present specific polarization patterns in the low frequency range, not common for all stations (see Polarization analysis). These caused huge orientation corrections, which would not be realistic. Thus, finally, no orientation corrections were applied.

The characteristics of the datasets are detailed in Tab. 3.

4.2 Data processing

The data were first converted to SAC format including in the header the coordinates of the point (CH1903 system), the recording component and a name related to the position. The name is made of 3 letters characterizing the location (MAU here), 1 digit for the ring and 2 more digits for the number in the ring (zero for the central station of the corresponding ring - if present). Recordings were not corrected for the instrumental response.

Dataset	Starting Date	Time	Length	F_s	Min. inter-distance	Aperture	# of points
1	2015/02/10	09:56	122 min	200 Hz	10 m	120 m	14
2	2015/02/10	14:21	131 min	200 Hz	10 m	400 m	14

Table 3: Usable datasets.

5 H/V processing

5.1 Processing method and parameters

In order to process the H/V spectral ratios, several codes and methods were used. The classical H/V method was applied using the Geopsy `http://www.geopsy.org` software. In this method, the ratio of the smoothed Fourier Transform of selected time windows are averaged. Tukey windows (cosine taper of 5% width) of $50\,\mathrm{s}$ long overlapping by 50% were selected. Konno and Ohmachi [1998] smoothing procedure was used with a b value of 60. The multitaper method of the spectra estimates [Prieto et al., 2009] was applied as well with the time bandwidth product of 2.5 and 4 tapers. The classical method of Fäh et al. [2001] was also performed.

Moreover, the time-frequency analysis method [Fäh et al., 2009] was used to estimate the ellipticity function more accurately using the Matlab code of V. Poggi. In this method, the time-frequency analysis using the Wavelet transform is computed for each component. For each frequency, the maxima over time (10 per minute with at least $0.1\,\mathrm{s}$ between each) in the TFA are determined. The Horizontal to Vertical ratio of amplitudes for each maximum is then computed and statistical properties for each frequency are derived. A Cosine wavelet with parameter 9 is used. The mean of the distribution for each frequency is stored. For the sake of comparison, the time-frequency analysis of Fäh et al. [2001], based on the spectrogram, was also used.

The ellipticity extraction using the wavefield decomposition method [Maranò et al., 2012] (see section on array analysis) was also performed.

Method	Freq. band	Win. length	Anti-trig.	Overlap	Smoothing
Standard H/V Geopsy	$0.2-20\,\mathrm{Hz}$	$50\,\mathrm{s}$	No	50%	K&O 60
Standard H/V Multitaper	$0.2-40\,\mathrm{Hz}$	$200\,\mathrm{s}$	No	-	-
Standard H/V D. Fäh	$0.2-20\,\mathrm{Hz}$	$30\,\mathrm{s}$	No	75%	-
H/V TFA D. Fäh	$0.2-20\,\mathrm{Hz}$	Specgram	No	-	-
H/V TFA V. Poggi	$0.2-20\,\mathrm{Hz}$	Cosine wpar=9	No	-	No

Table 4: Methods and parameters used for the H/V processing.

5.2 Results

All the methods to compute H/V ratios are compared at the array centre on Fig. 4, in which the classical methods were divided by $\sqrt{2}$ to correct from the Love wave contribution [Fäh et al., 2001]. Overall, the classical and TFA methods match well. Too strong smoothing can result in smearing of the fundamental peak.

All points of the array show similar same shape in their H/V with a pronounced peak (Fig. 5) between $0.5-2\,\mathrm{Hz}$. Nevertheless, a variability of the fundamental peaks is observed. This variability is systematic. The H/V curves for stations of the two innermost rings are shown in Fig. 6 together with the ellipticity curves for two modes obtained by the array Wavedec technique Maranò et al. [2012]. The fundamental peaks and right flanks of the ellipticity curves show good agreement in between the stations and the ellipticity of the fundamental mode obtained

with the array method, except stations MAU201 and MAU204. These two stations are located on the other side of the regulated Eschen stream (with respect to SMFL). The bump of H/V around $1.7\,\mathrm{Hz}$ might be attributed to the ellipticity peak of the first higher mode. The H/V ratios of points along a transverse cross section of the basin are shown in Fig. 7. A clear decreasing trend of the fundamental frequency ($1.3 - 0.8\,\mathrm{Hz}$) is observed from the South-East edge of the basin toward North-West. This indicates a likely assymetry of the basin (deeper at the North-West side). Note that the stations MAU404 and MAU504 located on the other side of the Eschen stream present again difference in the right flank of the H/V. Concluding, the fundamental peak at the SMFL station is at $1\,\mathrm{Hz}$, with a peak amplitude around 10 for the TFA methods.

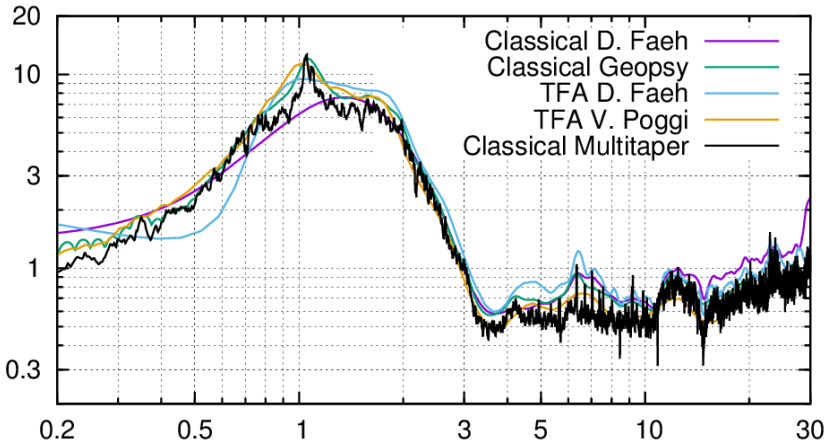

Figure 4: H/V spectral ratios for point MAU100 using the different codes. Classical methods were divided by $\sqrt{2}$.

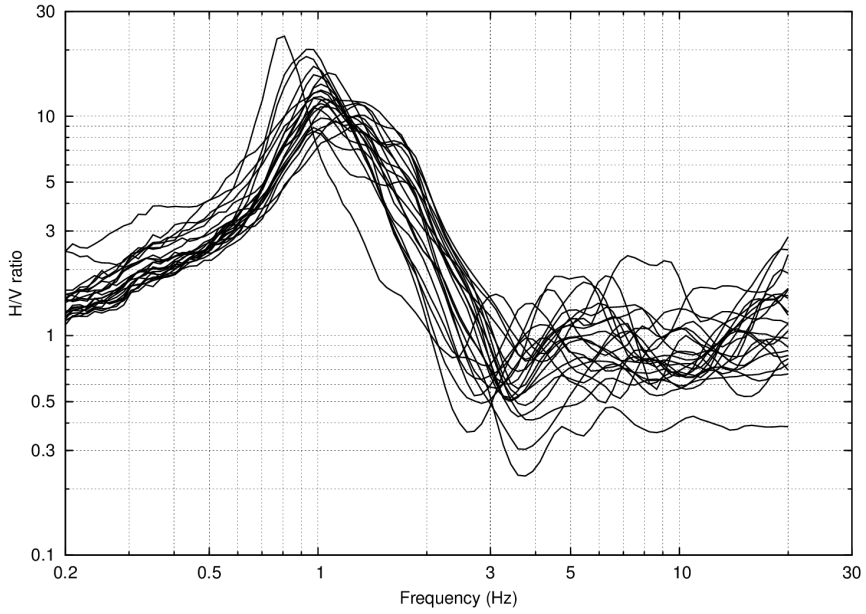

Figure 5: H/V spectral ratios (time-frequency analysis code V. Poggi).

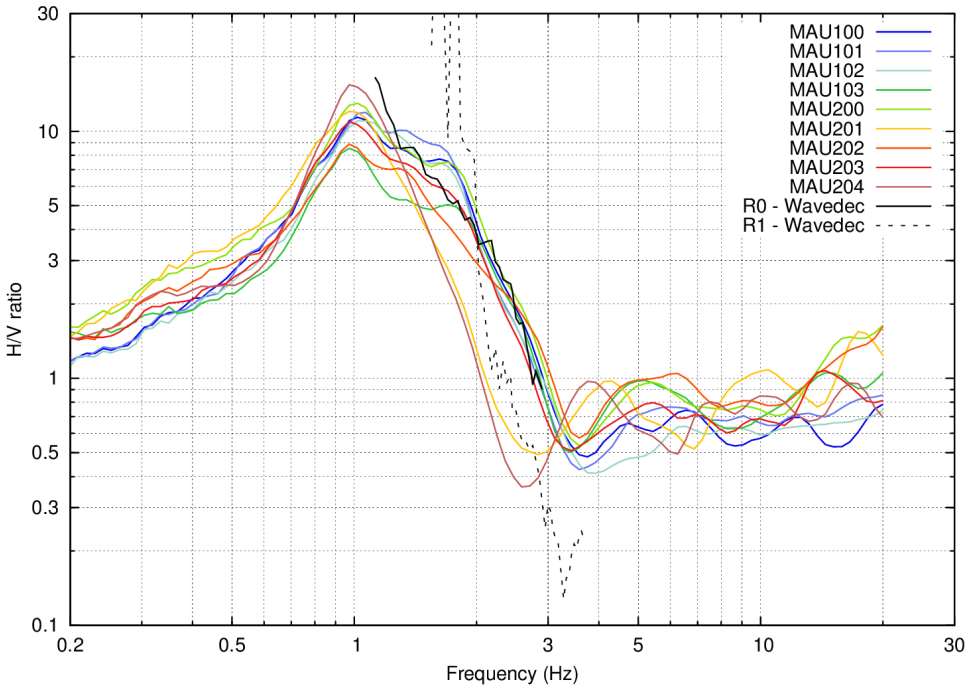

Figure 6: H/V spectral ratios for the two innermost rings. Ellipticity curves obtained by the array Wavedec technique are show in black.

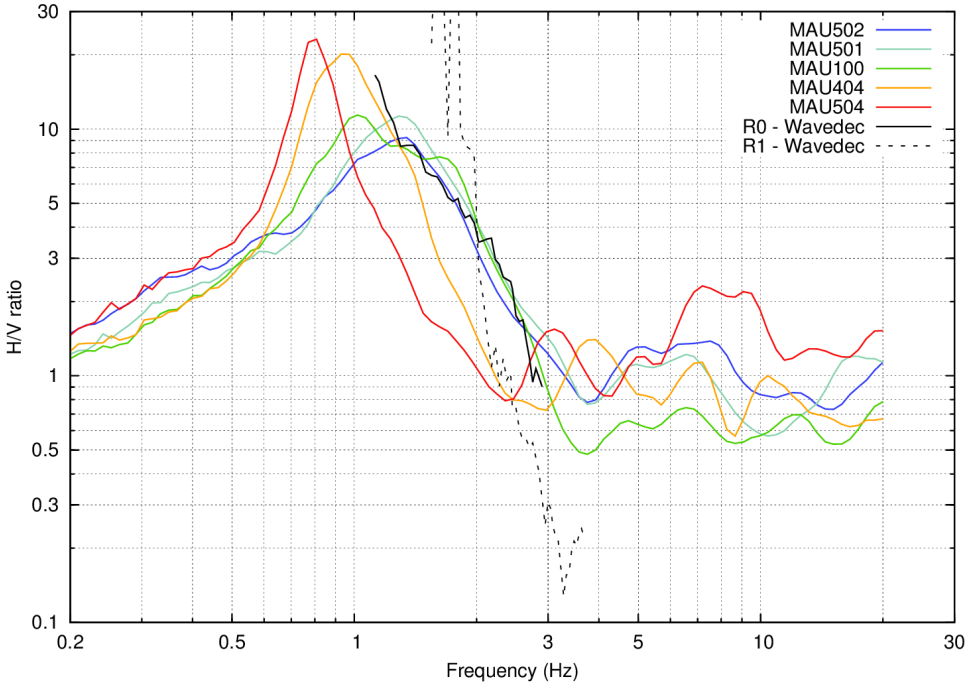

Figure 7: H/V spectral ratios for a cross-section of points traverse to the basin. Color temperature show the distance from South-East (SE) edge of the basin (blue - closest, red - furthermost from the SE edge). Ellipticity curves obtained by the array Wavedec technique are show in black.

5.3 Polarization analysis

Polarization analysis on the array data was performed using the method of Burjánek et al. [2010]. Most of the points (Fig. 8) show a particular polarization especially in the frequency band $1 - 3\,\mathrm{Hz}$. Clusters of points with similar polarization can be identified. For example, stations of the innermost ring (MAU100, MAU101, MAU102, MAU103) or stations on the other side of the Eschen stream (MAU201 ,MAU204). However, overall, it is difficult to make an interpretation, due to the strong variability. In general, such variability likely reflects lateral variability of the shallowest sediments, which might affected by human activities (construction works). The relative strong directionality of the surface propagation direction might have played role as well (retrieved during array processing, see below).

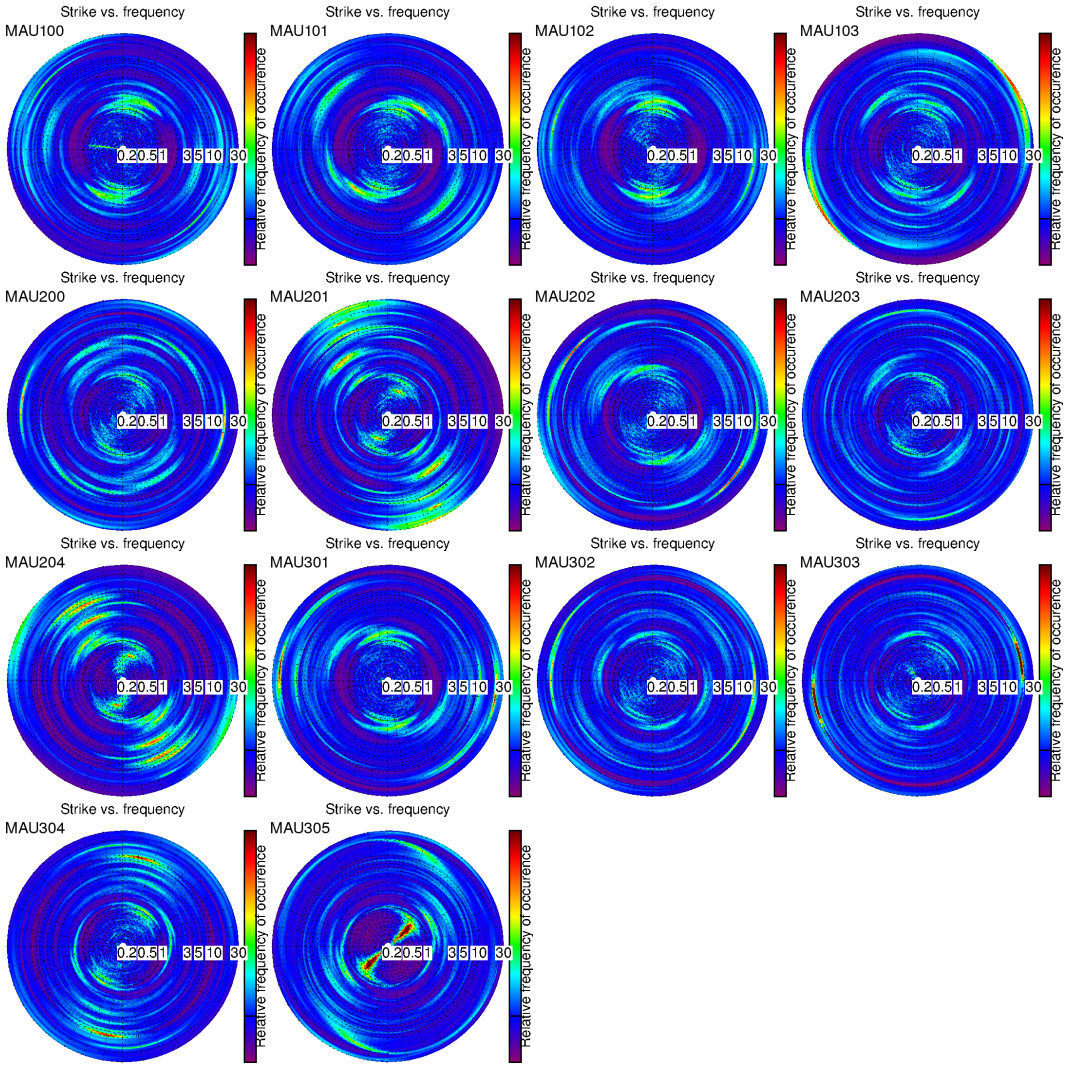

Figure 8: Strike of the polarization for all stations of the first array configuration (3 rings).

6 Array processing

6.1 Processing methods and parameters

The vertical components of the arrays were processed using the classical FK and the High-resolution FK (HRFK) analysis [Capon, 1969] using the Geopsy `http://www.geopsy.org` software. On one hand, in case of HRFK, better results were obtained using large time windows (300T). On the other hand, FK worked better with shorter time windows (50T). Moreover, a 3C array analysis [Fäh et al., 2008] was also performed using both the array_tool_3C software [Poggi and Fäh, 2010] (HRFK, FK) and Geopsy `http://www.geopsy.org` software (just FK). It allows to derive Rayleigh and Love modes including the Rayleigh ellipticity. Finally, 3C array Wavedec technique was applied as well [Maranò et al., 2012].

Method	Set	Freq. band	Win. length	Anti-trig.	Overlap	Grid step	Grid size	# max.
HRFK 1C	1	$0.5 - 10\,\mathrm{Hz}$	$100T$	No	50%	0.0033	1.363	2
HRFK 1C	2	$0.5 - 10\,\mathrm{Hz}$	$300T$	No	50%	0.0009	0.885	2
FK 1C	2	$0.5 - 10\,\mathrm{Hz}$	$50T$	No	50%	0.0045	0.885	2
FK 3C	1	$0.5 - 10\,\mathrm{Hz}$	$50T$	No	50%	0.0193	0.927	2

Table 5: Methods and parameters used for the array processing.

6.2 Obtained dispersion curves

The interpretation was not straightforward, as some of the methods did not provide very useful results for these datasets. Selected results of the different FK analysis are presented in Fig. 9 together with final picks. Surprisingly, simple FK 3C analysis of the first configuration provided most of the results (Rayleigh fundamental mode could be picked between 2 - $3.5\,\mathrm{Hz}$, Rayleigh 1st higher mode could be picked between 2.5 - $4\,\mathrm{Hz}$, Love mode between 1 - $5\,\mathrm{Hz}$. 1C HRFK of the first configuration extended fundamental Rayleigh mode down to $1.5\,\mathrm{Hz}$. 1C HRFK of the second configuration allowed to improve and extend 1st higher Rayleigh mode between 2 - $4\,\mathrm{Hz}$.

Here we discuss shortly the unsuccessful trials. In general HRFK methods tend to pick up only the 1st higher Rayleigh mode, suppressing completely the both Love and Rayleigh fundamental modes. Only exception was frequency range between 1.5 - $2\,\mathrm{Hz}$, where the fundamental Rayleigh mode was more dominating (positive result with 1C HRFK). Radial component was heavily affected by Love fundamental mode, especially below the lower resolution limit in case of 3C BF. Similarly, Wavedec technique provided Rayleigh fundamental mode shifted towards the Love fundamental mode. The second array configuration provided only Rayleigh 1st higher mode, no fundamental modes were observed. Based on the results of the inversion (see below), the Rayleigh 1st higher mode is in this specific case mainly influenced by the deeper part of the basin, which might be more homogeneous over the area.

The directionality of the wavefield is shown in Fig. 10 and Fig. 11. In particular, the different plots show maxima picked from the FK plane considering different ranges of directions of

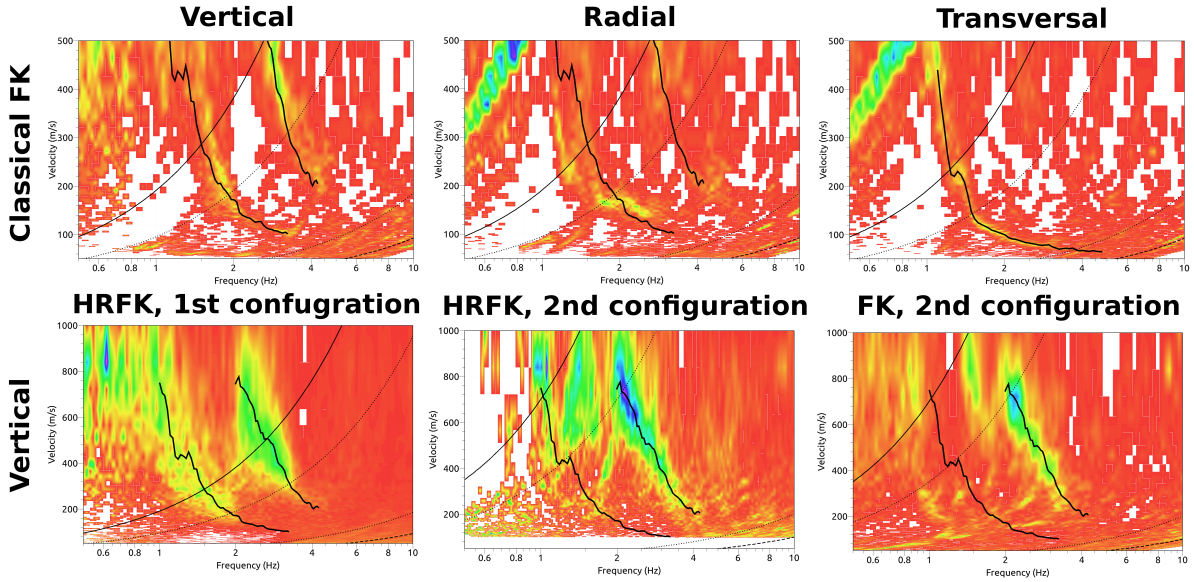

Figure 9: Dispersion curves from the 3C and 1C array analyses (Top: 3C classical FK analysis of the first configuration; Bottom: 1C HRFK analysis of the first configuration + 1C HRFK & FK analysis of the second configuration).

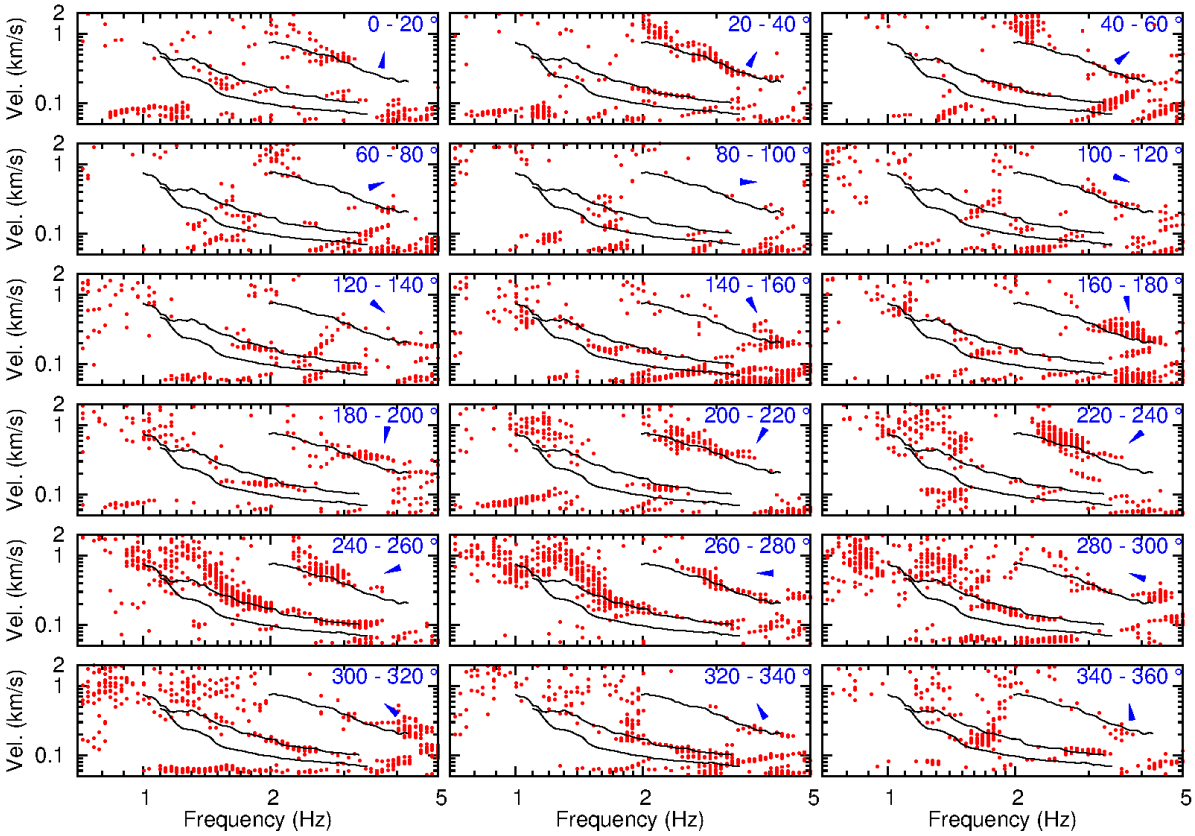

Figure 10: Directionality of the vertical component of the wavefield based on 3C classical FK analysis. Red dots are the maxima picked from the FK plane, both Love & Rayleigh picked dispersion curves are in black. The numbers in blue show the range of directions of the wave propagation, denoted by blue arrow as well.

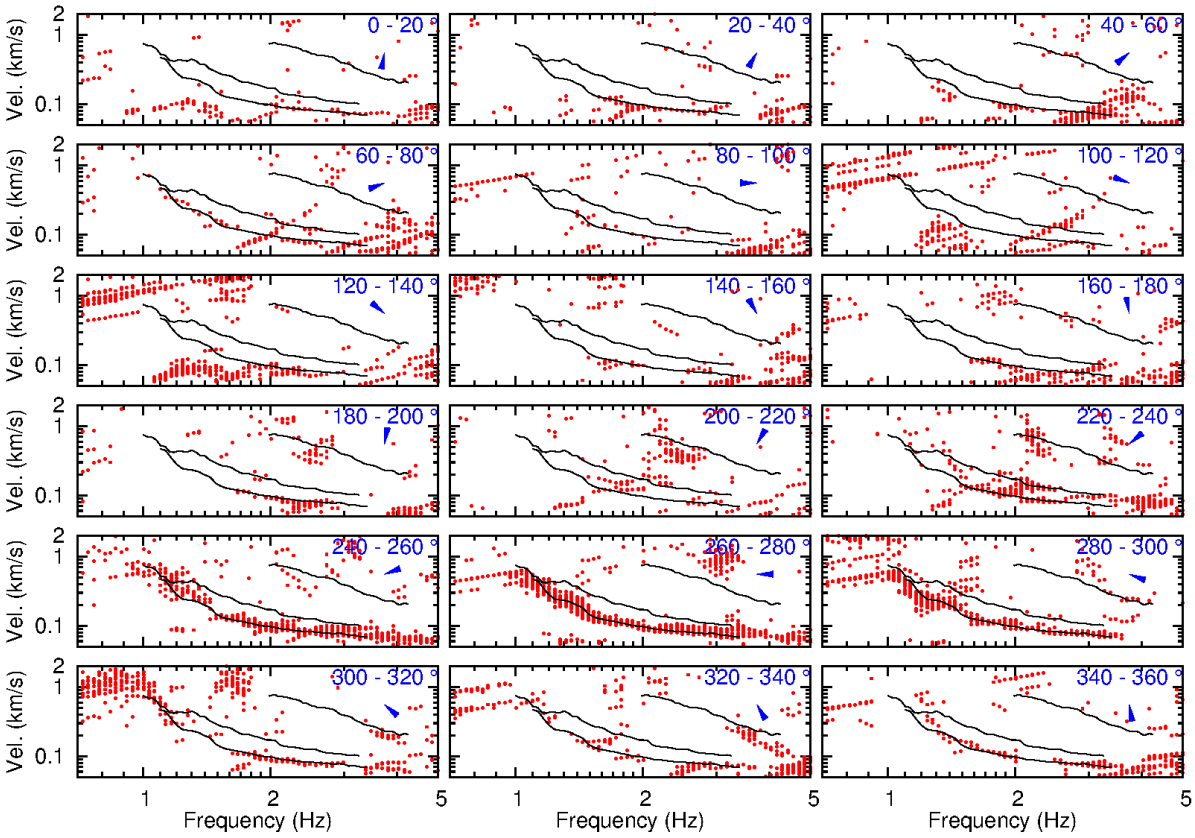

Figure 11: Directionality of the transverse component of the wavefield based on 3C classical FK analysis. Red dots are the maxima picked from the FK plane, both Love & Rayleigh picked dispersion curves are in black. The numbers in blue show the range of directions of the wave propagation, denoted by blue arrow as well.

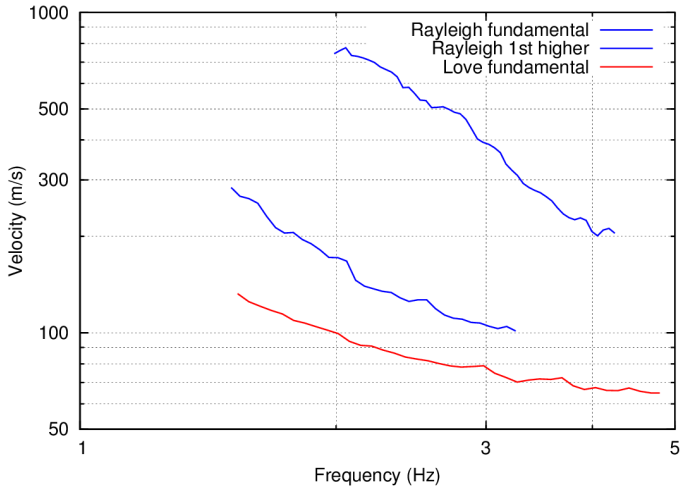

Figure 12: Picked dispersion curves from 1C and 3C FK methods.

the wave propagation. The picked dispersion curves are based mainly on the waves traveling towards west, i.e., generated likely in the industrial area to the east of the array. Such strong directional distribution of the sources might explain the strong polarization features discussed earlier. There is almost no contribution from the west and north-west, which might indicate a potential lateral boundary aligned with the Eschen stream (note the difference in the polarization diagrams and H/V curves, on the other side of the Eschen stream).

All picked curves, trimmed according to the resolution limits, are presented together on Fig. 12.

7 Inversion and interpretation

7.1 Inversion

For the inversion, Rayleigh 1st higher, fundamental and Love fundamental mode dispersion curves between 1.5 and $5\,\mathrm{Hz}$, as well as the ellipticity of the fundamental mode were used as simultaneous targets without standard deviation to avoid different weighting. The first higher mode ellitpicity obtained with Wavedec technique was not used in the inversion as it was subjected to a very high uncertainty. A weight of 0.5 was assigned to the ellipticity curve. All curves were resampled using 80 points between 0.2 and $6\,\mathrm{Hz}$ in log scale.

The inversion was performed using the Improved Neighborhood Algorithm (NA) Wathelet [2008] implemented in the Dinver software. In this algorithm, the tuning parameters are the following: Ns_0 is the number of starting models, randomly distributed in the parameter space, Nr is the the number of best cells considered around these Ns_0 models, Ns is the number of new cells generated in the neighborhood of the Nr cells (Ns/Nr per cell) and It_{max} is the number of iteration of this process. The process ends with $Ns_0 + Nr * \frac{Ns}{Nr} * It_{max}$ models. The used parameters are detailed in Tab. 6.

It_{max}	Ns_0	Ns	Nr
200	10000	800	400

Table 6: Tuning parameters of Neighborhood Algorithm.

The velocity was assumed to increase with depth. The Poisson ratio was inverted in each layer in the range 0.2-0.45. The density was assumed between 2000 and $2600\,\mathrm{kg/m^3}$. A number of inversions with fixed layer depths were performed (testing different parametrizations). Four different parametrization schemes were finally considered (reducing consequently the number of the fixed depth layers in the deeper part of the model - from 19 to 10). Fine layering close to the surface was introduced, to capture the shallow strong interface. For further elaborations, the 10 best models of these 4 runs were selected (Fig. 14).

We found a first layer of approximately $12\,\mathrm{m}$ with extremely low shear wave velocities of about $70\,\mathrm{m/s}$ corresponding to unconsolidated soil. This part of the profile is mainly constrained by the both Love and Rayleigh fundamental mode dispersion curves and peak of the ellipticity of the fundamental mode. A rapid increase of velocities to $300 - 400\,\mathrm{m/s}$ is found at depths of $12 - 15\,\mathrm{m}$. Below the velocity is increasing up $500 - 900\,\mathrm{m/s}$ down to the bedrock. This part of the model is mainly constrained by the first higher Rayleigh mode dispersion curve and ellipticity of the fundamental mode (both peak and curve). The bedrock depth is not well constrained, but the data suggest the minimum depth of $100\,\mathrm{m}$.

The dispersion curves are well represented, and the ellipticity curve is satisfactorily reproduced as well.

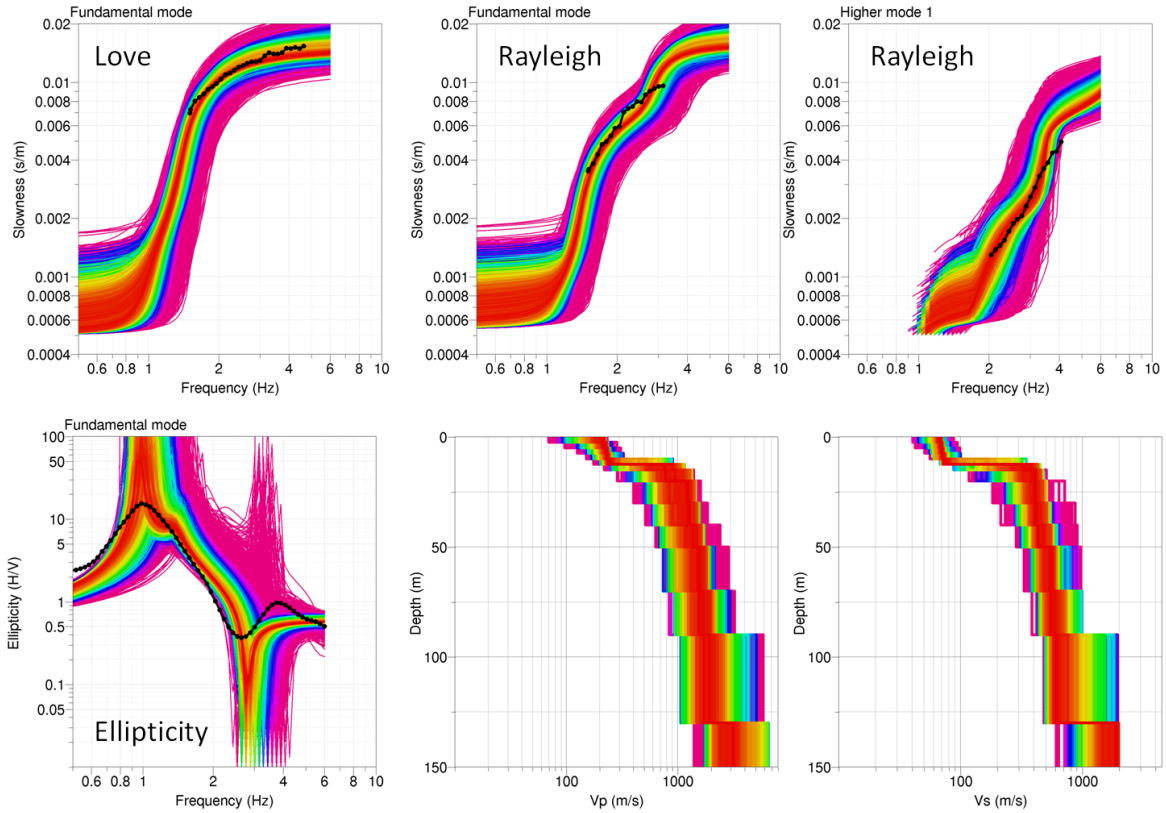

Figure 13: Comparison between inverted and measured Rayleigh, Love modes, ellipticity curves. Corresponding inverted ground profiles in terms of V_p and V_s are plotted in bottom-right.

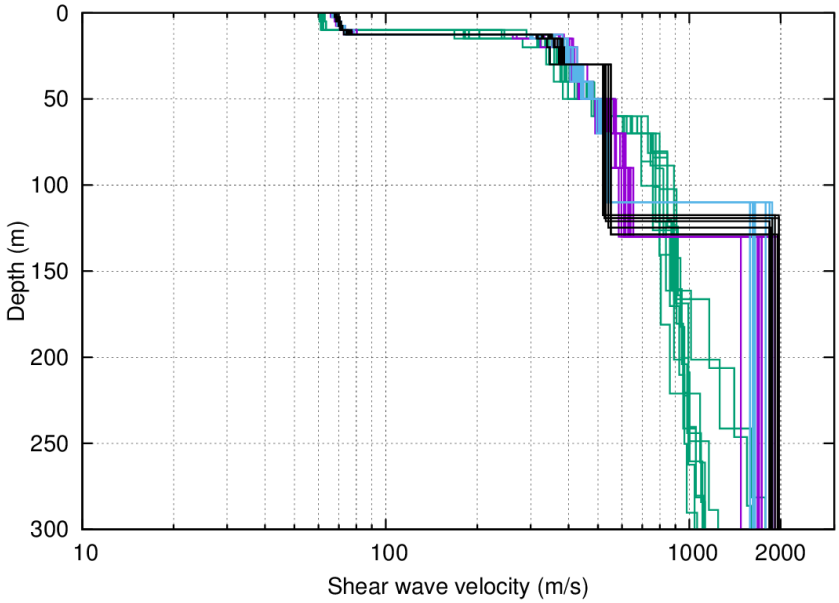

Figure 14: V_s ground profiles for the selected 40 best models. Different colors distinguish different parametrizations.

7.2 Travel time average velocities and ground type

The distribution of the travel time average velocities at different depths was computed from the selected models. The uncertainty, computed as the standard deviation of the distribution of travel time average velocities for the considered models, is also provided, but it is not guaranteed that the full range of uncertainties is covered. $V_{s,30}$ is found to be $134\,\mathrm{m/s}$, which would generally correspond to ground type D in the Eurocode 8 [CEN, 2004], and D for the SIA261 [SIA, 2014]. However, the special ground types S1, S2 of Eurocode 8 or type F of the SIA261 [SIA, 2014] should be consider in this case, as the first layer is relatively thick ($12\,\mathrm{m}$) and does not show normal consolidation.

	Mean (m/s)	**Uncertainty (m/s)**
$V_{s,5}$	67	3
$V_{s,10}$	68	3
$V_{s,20}$	101	1
$V_{s,30}$	134	2
$V_{s,40}$	162	3
$V_{s,50}$	186	4
$V_{s,100}$	281	4

Table 7: Travel time averages at different depths from the inverted models. Uncertainty is given as one standard deviation from the selected profiles.

7.3 SH transfer function and quarter-wavelength velocity

The quarter-wavelength velocity approach [Joyner et al., 1981] provides, for a given frequency, the average velocity at a depth corresponding to 1/4 of the wavelength of interest. It is useful to identify the frequency limits of the experimental data (minimum frequency in dispersion curves at $1.5\,\mathrm{Hz}$ and ellipticity peak at $1\,\mathrm{Hz}$ here). The results using this proxy show that the dispersion curves constrain the profiles down to $20\,\mathrm{m}$ and the ellipticity down to $40\,\mathrm{m}$ (Fig. 15). Moreover, the quarter wavelength impedance-contrast introduced by Poggi et al. [2012a] is also displayed in the figure. It corresponds to the ratio between two quarter-wavelength average velocities, respectively from the top and the bottom part of the velocity profile, at a given frequency [Poggi et al., 2012a]. It shows a trough (inverse shows a peak) at the resonance frequency.
Moreover, the theoretical SH-wave transfer function for vertical propagation [Roesset, 1970] is computed from the inverted profiles. It is compared to the quarter-wavelength amplification [Joyner et al., 1981] that however cannot take resonances into account (Fig. 16). In this case, the models are predicting a peaky amplification up to a factor of 10 at several resonance peaks between 1 and $10\,\mathrm{Hz}$.

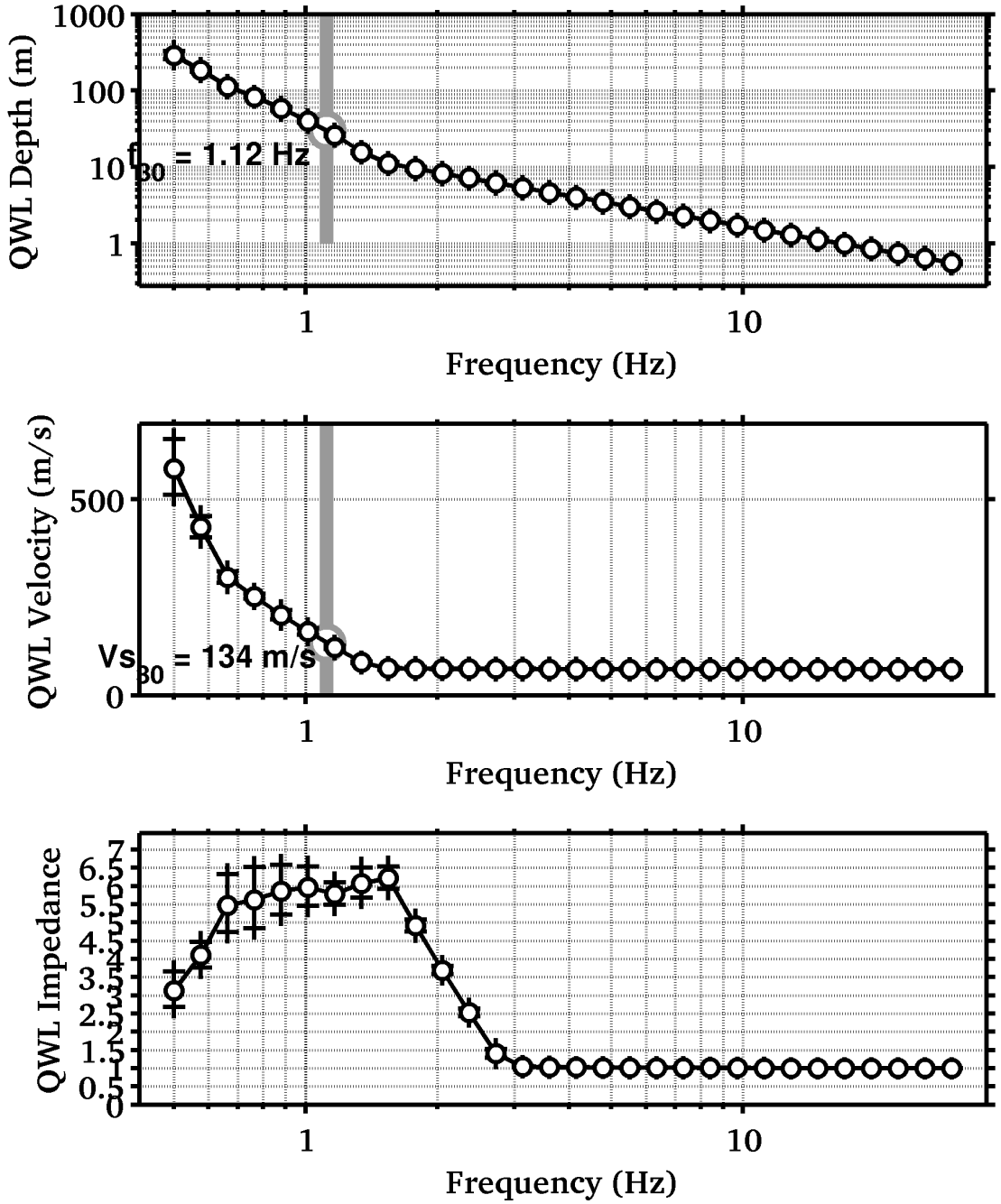

Figure 15: Quarter wavelength velocity representation of the velocity profile (top: depth, centre: velocity, bottom: inverse of the impedance contrast). Grey bar corresponds to $V_{s,30}$.

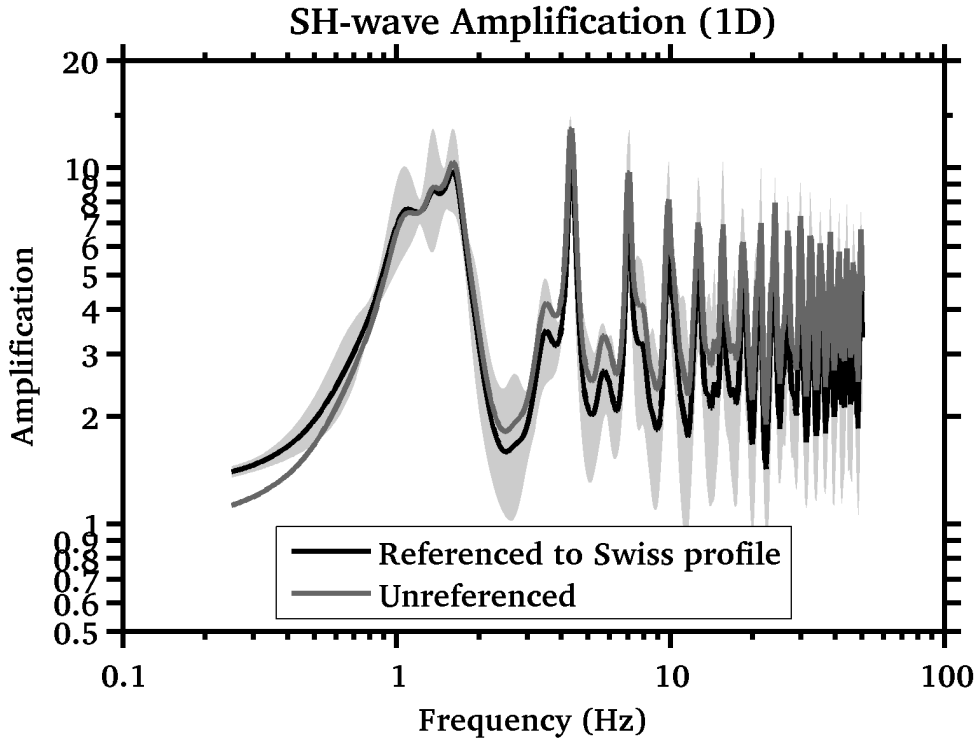

Figure 16: Theoretical SH transfer function (solid line) and quarter wavelength impedance contrast (dashed line) with their standard deviation. Significance of the greyshades is detailed in Fig. 15.

8 Conclusions

The array measurements presented in this study were successful in deriving a velocity model for the site of the SMFL station. We found a first layer of approximately $12\,\mathrm{m}$ with extremely low shear wave velocities of about $70\,\mathrm{m/s}$ corresponding to unconsolidated soil. A rapid increase of velocities to $300-400\,\mathrm{m/s}$ is found at depths of $12-15\,\mathrm{m}$. Below the velocity is increasing up $500-900\,\mathrm{m/s}$ down to the bedrock. The bedrock depth is not well constrained, but the data suggest the minimum depth of $100\,\mathrm{m}$.
$V_{s,30}$ is $134\,\mathrm{m/s}$ would generally correspond to ground type D in the Eurocode 8 [CEN, 2004], and D for the SIA261 [SIA, 2014]. However, the special ground types S1, S2 of Eurocode 8 or type F of the SIA261 [SIA, 2014] should be consider in this case, as the first layer is relatively thick ($12\,\mathrm{m}$) and does not show normal consolidation. A further geotechnical study (like CPT) of the uppermost layer would be required for the more specific classification. The theoretical 1D SH transfer function and impedance contrast of the quarter-wavelength velocity computed from the inverted profiles show significant amplifications at clearly defined resonance frequencies. Recordings on the new station will allow to compare to these simple models.

Acknowledgements

The authors thank Oona Brunner and Jiri Vackar who helped with the measurement.

References

Sylvette Bonnefoy-Claudet, Fabrice Cotton, and Pierre-Yves Bard. The nature of noise wavefield and its applications for site effects studies. *Earth-Science Reviews*, 79(3-4): 205–227, December 2006. ISSN 00128252. doi: 10.1016/j.earscirev.2006.07.004. URL http://linkinghub.elsevier.com/retrieve/pii/S0012825206001012.

Jan Burjánek, Gabriela Gassner-Stamm, Valerio Poggi, Jeffrey R. Moore, and Donat Fäh. Ambient vibration analysis of an unstable mountain slope. *Geophysical Journal International*, 180(2):820–828, February 2010. ISSN 0956540X. doi: 10.1111/j.1365-246X.2009.04451.x. URL http://gji.oxfordjournals.org/cgi/doi/10.1111/j.1365-246X.2009.04451.xhttp://doi.wiley.com/10.1111/j.1365-246X.2009.04451.x.

J. Capon. High-Resolution Frequency-Wavenumber Spectrum Analysis. *Proceedings of the IEEE*, 57(8):1408–1418, 1969. ISSN 0018-9219. doi: 10.1109/PROC.1969.7278. URL http://ieeexplore.ieee.org/lpdocs/epic03/wrapper.htm?arnumber=1449208.

CEN. *Eurocode 8: Design of structures for earthquake resistance - Part 1: General rules, seismic actions and rules for buildings*. European Committee for Standardization, en 1998-1: edition, 2004.

Donat Fäh, Fortunat Kind, and Domenico Giardini. A theoretical investigation of average H/V ratios. *Geophysical Journal International*, 145(2):535–549, May 2001. ISSN 0956540X. doi: 10.1046/j.0956-540x.2001.01406.x. URL http://doi.wiley.com/10.1046/j.0956-540x.2001.01406.x.

Donat Fäh, Gabriela Stamm, and Hans-Balder Havenith. Analysis of three-component ambient vibration array measurements. *Geophysical Journal International*, 172(1):199–213, January 2008. ISSN 0956540X. doi: 10.1111/j.1365-246X.2007.03625.x. URL http://doi.wiley.com/10.1111/j.1365-246X.2007.03625.xhttp://gji.oxfordjournals.org/cgi/doi/10.1111/j.1365-246X.2007.03625.x.

Donat Fäh, Marc Wathelet, Miriam Kristekova, Hans-Balder Havenith, Brigitte Endrun, Gabriela Stamm, Valerio Poggi, Jan Burjánek, and Cécile Cornou. Using Ellipticity Information for Site Characterisation. Technical report, NERIES JRA4 Task B2, 2009.

William B. Joyner, Richard E. Warrick, and Thomas E. Fumal. The effect of Quaternary alluvium on strong ground motion in the Coyote Lake, California, earthquake of 1979. *Bulletin of the Seismological Society of America*, 71(4):1333–1349, 1981.

Katsuaki Konno and Tatsuo Ohmachi. Ground-Motion Characteristics Estimated from Spectral Ratio between Horizontal and Vertical Components of Microtremor. *Bulletin of the Seismological Society of America*, 88(1):228–241, 1998.

Stefano Maranò, C. Reller, H.-A. Loeliger, and Donat Fäh. Seismic waves estimation and wave field decomposition: Application to ambient vibrations. *Geophysical Journal International*, submitted, 2012.

Valerio Poggi and Donat Fäh. Estimating Rayleigh wave particle motion from three-component array analysis of ambient vibrations. *Geophysical Journal International*, 180(1):251–267, January 2010. ISSN 0956540X. doi: 10.1111/j.1365-246X.2009.04402.x. URL http://doi.wiley.com/10.1111/j.1365-246X.2009.04402.x.

Valerio Poggi, Benjamin Edwards, and Donat Fäh. Characterizing the Vertical-to-Horizontal Ratio of Ground Motion at Soft-Sediment Sites. *Bulletin of the Seismological Society of America*, 102(6):2741–2756, December 2012a. ISSN 0037-1106. doi: 10.1785/0120120039. URL http://www.bssaonline.org/cgi/doi/10.1785/0120120039.

Valerio Poggi, Donat Fäh, Jan Burjánek, and Domenico Giardini. The use of Rayleigh-wave ellipticity for site-specific hazard assessment and microzonation: application to the city of Lucerne, Switzerland. *Geophysical Journal International*, 188(3):1154–1172, March 2012b. ISSN 0956540X. doi: 10.1111/j.1365-246X.2011.05305.x. URL http://doi.wiley.com/10.1111/j.1365-246X.2011.05305.xhttp://gji.oxfordjournals.org/cgi/doi/10.1111/j.1365-246X.2011.05305.x.

G.A. Prieto, R.L. Parker, and F.L. Vernon III. A fortran 90 library for multitaper spectrum analysis. *Computers & Geosciences*, 35(8):1701 – 1710, 2009. ISSN 0098-3004. doi: http://dx.doi.org/10.1016/j.cageo.2008.06.007. URL http://www.sciencedirect.com/science/article/pii/S0098300409000077.

J.M. Roesset. Fundamentals of soil amplification. In R. J. Hansen, editor, *Seismic Design for Nuclear Power Plants*, pages 183–244. M.I.T. Press, Cambridge, Mass., 1970. ISBN 978-0-262-08041-5. URL http://mitpress.mit.edu/catalog/item/default.asp?ttype=2&tid=5998.

SIA. *SIA 261 Einwirkungen auf Tragwerke*. Schweizerischen Ingenieur- und Architektenverein, Zürich, sia 261:2014 edition, 2014.

Marc Wathelet. An improved neighborhood algorithm: Parameter conditions and dynamic scaling. *Geophysical Research Letters*, 35(9):1–5, May 2008. ISSN 0094-8276. doi: 10.1029/2008GL033256. URL http://www.agu.org/pubs/crossref/2008/2008GL033256.shtml.